THE FINITE ELEMENT METHOD ANALYSIS OF TEMPERATURE DISTRIBUTION OF THE FAMA ELECTRON CYCLOTRON RESONANCE MINI-OVEN

by

Igor N. TELEČKI*, Ljubiša T. VUKOSAVLJEVIĆ, Ivan M. TRAJIĆ, Marko V. ERICH, and Viktor N. JOCIĆ

Department of Physics, Vinča Institute of Nuclear Sciences,
National Institute of the Republic of Serbia, University of Belgrade, Belgrade, Serbia

Original scientific paper
https://doi.org/10.2298/TSCI210519235T

The mVINIS ion source, a part of FAMA installation at Vinča Institute of Nuclear Sciences, is able to produce multiple charged heavy ion beams through the utilization of vapors created by the process of melting solids inside the miniature oven (mini-oven). The mini-oven that was used previously could only reach the maximum temperature of 800 °C, which is far too low for evaporating most metals. For this purpose, a higher operating-temperature of 1500 °C was needed. Our study focuses on numerical finite element method analysis of the temperature distribution of newly designed mini-oven.

Key words: *oven, ion beam, evaporate, finite element method*

Introduction

The mVINIS ion source is part of FAMA installation (*Facility for Modification and Analysis of Materials with Ion Beams*) at the Vinča Institute of Nuclear Sciences, Belgrade, Serbia [1]. The mVINIS source can produce the highly charged ions via the micro-wave heating of the plasma on electron cyclotron resonance frequencies, the so called ECR source. It gives a wide variety of ion beams ranging from standard gases, such as He, N, O, Ne, Ar, Kr, and Xe to solids, like Zn, Pb, B, and Fe [2-4]. The metal ion beams are produced from metallic vapors created by two different methods:

– melting of metals in mini-oven [5, 6] and
– the MIVOC (metal ions from volatile compounds) method [7, 8].

The former method is often used for obtaining ions out of metals with relatively low melting temperature, such as Pb, while the later one is used for obtaining ions out of metals with high melting temperature metals by utilizing evaporating organic compounds containing the desired metal instead. However, MIVOC method has a major drawback of high ECR source pollution, which then calls for long period of ion source maintenance preventing its experimental use. Additionally, these organic compounds tend to be expensive. Therefore, a significantly cleaner method of metal evaporation through the melting process with the mini-oven is a more desirable way. However, a higher heating temperature than 800 °C is needed, for instance, 860 °C for Ag or 1300 °C for Ni.

Figure 1 depicts the mVINIS ECR source with solid substance inlet system. The mini-oven with the solid material is inserted through the bias electrode at the edge of the plas-

* Corresponding author, e-mail: teligor74@gmail.com

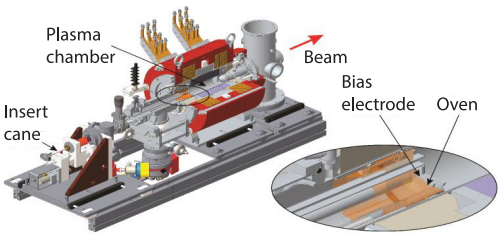

Figure 1. A 3/4 cross-sectional view of the FAMA ECR ion source with solid substance inlet system

ma chamber. This is accomplished by having the mini-oven connected to the long stainless-steel cane, which allows the insertion of the mini-oven slightly out of the axis of the ion source. The solid substance in the mini-oven is electrically heated to the melting point. The heater temperature is determined indirectly from the heater power consumption, using the measured calibration temperature vs. mini-oven power curve.

The original mini-oven [9] has a maximum heating temperature of 800 °C. For this reason two new mini-ovens have been acquired from PANTECHNIK [10]. During the testing with lead, tungsten filaments on both mini-ovens had burned out after three hours of continuous work, not reaching temperature of 700 °C. In view of this, we have opted for the construction of our own mini-oven with maximum temperature of 1500 °C in the alumina-made crucible. The maximum temperature limiting factor for the design is the chemical reaction between tungsten-made filament and alumina-made crucible which occurs at 1700 °C, the highest temperature allowed on the filament, which translates to 1500 °C in the crucible itself [11]. In order to test whether our mini-oven design could reach the desired working temperatures in steady-state, the numerical FEM analysis has been performed using the COMSOL heat transfer module interface [12]. From it, the mini-oven temperature distribution was obtained.

The FAMA mini-oven design

The mini-oven design is shown in fig. 2(a). The heater subassembly – 1 is placed inside the insulation cladding made of alumina – 5 and 6. Mini oven body parts – 2 and 3 are made of tantalum. Oven body on its back side is connected to the cane assembly – 9 by the connector piece – 8. The electrical contact between the heater subassembly and the copper conductor inside the cane assembly was realized through a terminal block – 7. The heater subassembly, shown in fig. 2(b), consists of: an alumina-made crucible – 10, a tungsten-made filament – 11, a molybdenum-made electrical connectors – 12 and 13, and an alumina-made oven tip – 14. The inner diameter of the crucible is 3 mm while its length is 28 mm. At the both ends of the crucible, filament feedthroughs with 1 mm in diameter, have been drilled. The filament has a total of 30 windings with a step of 1 mm. An additional extension has been mounted on the oven top – 14 which to prevents deposition of an evaporated substance on mini-oven's outer layer. Sufficient gaps are left between oven components so as to avoid the occurrence of contact stress induced by thermal dilatations. The outer diameter of the mini-oven is 9.2 mm its total length is 83 mm, with the weight of 46 g. The oven mockup model was made in 1:1 scale for the purpose of production and assembling feasibility study.

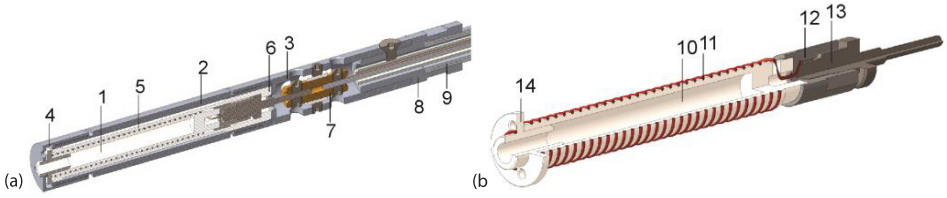

Figure 2. The FAMA mini-oven assembly: *1 – heater subassembly, 2 and 3 – oven bodies, 4 – cover, 5 and 6 – insulation claddings, 7 – terminal block, 8 – cane connector, 9 – cane assembly, 10 – crucible, 11 – filament, 12, 13 – connectors, and 14 – oven tip*

Heat transfer mechanisms

Heat transfer is the process of heat energy exchange between thermodynamic systems at different temperatures. Heat transfer is classified into various mechanisms such as thermal conduction, thermal convection, thermal radiation and energy transfer via phase change. Mini-oven was designed operate in a vacuum. Therefore, only thermal conduction and radiation have been considered in our case**.** The heat transfer equation is a PDE that determines the distribution of heat in space and time. In a steady-state case, the heat equation has the following differential form:

$$-k\Delta T = Q \tag{1}$$

where k is the material's thermal conductivity and Δ – the Laplace operator

$$\Delta = \left(\frac{\partial}{\partial^2 x} + \frac{\partial}{\partial^2 y} + \frac{\partial}{\partial^2 z} \right)$$

while Q [Wm^{-3}] is the internal heat generation rate per unit of volume. The heat equation, eq. (1), accepts two basic types of boundary conditions: specified temperature and specified heat flux, the so called Dirichlet and von Neumann boundary conditions, respectively:

$$T = T_0 \tag{2a}$$

$$\vec{n} \cdot \vec{q} = q_0 \text{ on } \partial \sum \tag{2b}$$

where T_0 denotes the external temperature on a boundary surface, $\partial\sum$, $\vec{q}$ [Wm^{-2}] – the heat flux vector, $\vec{n}$ – the boundary normal vector, and q_0 – the inward heat flux. The inward heat flux is a sum of all heat transfer mechanisms, that is conduction, q_{cn}, and radiation, q_r, respectively.

In the case of heat exchange by conduction, the internal heat transfer occurs between two points of the same body or two bodies in contact. The Fourier's law of thermal conduction shows that heat flux, q, is equal to the product of thermal conductivity coefficient, k, and the negative temperature gradient, $\vec{\nabla} T$:

$$q_{cn} = -k\vec{\nabla} T \tag{3}$$

The heat fluxes originating from two solid bodies in contact, with temperatures T_1 and T_2 at their interface, determine von Neumann boundary conditions, which in this case are:

$$-\vec{n}_1 q_1 = h\left(T_1 - T_2\right) \text{ on } \partial \sum\nolimits_1 \tag{4a}$$

$$-\vec{n}_2 q_2 = h\left(T_2 - T_1\right) \text{ on } \partial \sum\nolimits_2 \tag{4b}$$

where h is a joint conductance, which is in our case a sum of two contributions, h_c – the constriction conductance from the contact spots, and h_r – the radiative conductance. We have used Cooper-Mikic-Yovanovich (CMY) correlation [13] for constriction conductance, h_c. The CMY model considers plastic deformation, Gaussian height distribution of surface asperities (profile and slopes), isotropic surface and random distribution of the asperities in contact area. The resulting correlation according to CMY model:

$$h_c = 1.25 k_{contact} \frac{m_{asp}}{\sigma_{asp}} \left(\frac{p}{H_c} \right)^{0.95} \tag{5}$$

where $k_{contact} = 2k_1k_2/(k_1+k_2)$ is the harmonic mean of the thermal conductivities of surfaces 1 and 2, σ_{asp} – the surface roughness, and m_{asp} – average surface slope, p – the contact pressure, and H_c – the effective elastic micro-hardness.

The radiative conductance, h_r, for gray-diffuse parallel plate model, such as in our case, is given:

$$h_r = \frac{\varepsilon_1\varepsilon_2}{\varepsilon_1+\varepsilon_2-\varepsilon_1\varepsilon_2}\sigma\left(T_1^3+T_2^2T_1+T_2T_1^2+T_2^3\right) \tag{6}$$

where $s = 5.6706 \cdot 10^{-8}$ [Wm^{-2}K^{-2}] is the Stefan–Boltzmann constant and ε_1 and ε_2 are the emissivities of materials of both contact surfaces.

For the case of two bodies in contact, fig. 3(a), the orthogonal conductive thermal flux between them is $q_x = (T_2 - T_1)/(L_1/k_1S + L_2/k_2S + 1/hS)$, where S is the contact area while L_1 and L_2 are body lengths measured from the interface. The effective influence of thermal contact between body 1 and 2 on thermal conductivity flux can be represented as a third body between them with thermal resistance $1/hS$ shown in fig. 3(b).

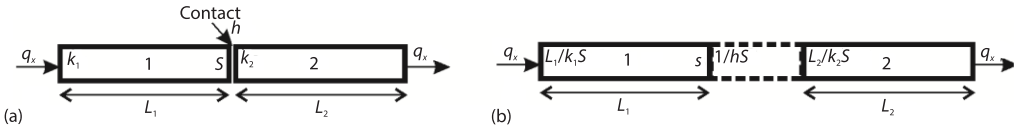

Figure 3. (a) Thermal flux between two solid bodies in contact and (b) effective thermal contact represented as a new body (dashed lines) with thermal resistance $R = 1/(h_c + h_s)S$

The second mechanism for heat transfer in our case is radiation. Thermal radiation denotes the stream of electromagnetic waves emitted from a body at a certain temperature. According to the Stefan-Boltzmann's law, the heat flux that body radiates across all wavelengths is a forth power of the body's temperature:

$$q_{SB} = \varepsilon n^2 \sigma T^4 \tag{7}$$

where ε is the surface material emissivity ranging from 0 to 1, n – the refractive index of the medium, equal to 1 in vacuum, σ – Stefan-Boltzmann's constant, and T – body temperature. The emissivity represents the material effectiveness in emitting thermal radiation, and is the ratio of the thermal radiation emitted from a surface of a body to one emitted from an ideal black body at the same temperature. The radiative heat flux q_r, is defined as the difference between incident radiation – irradiation G, and emitted radiation – radiosity J:

$$q_r = G - J \tag{8}$$

Radiosity is defined as a sum of reflected incident radiation, ρG (ρ is the reflexivity), and emitted heat radiation, fig. 4. In the case of grey opaque bodies, such as is in our case, the emissivity, ε, and the absorptivity, α, are equal while radiation is not transmitted through the body, therefore, radiosity is given:

$$J = (1-\varepsilon)G + \varepsilon n^2 \sigma T^4 \tag{9}$$

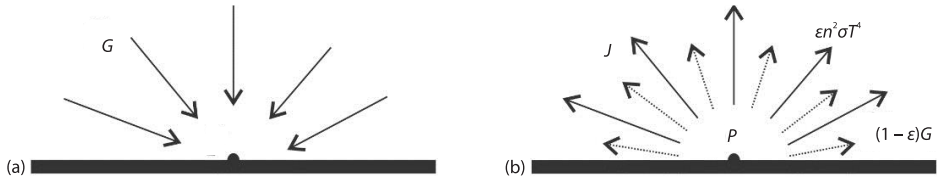

Figure 4. An ideal opaque gray body; (a) incoming irradiation, G, and (b) outgoing radiosity, J, is a sum of reflected, $(1-\varepsilon)G$, and emitted radiation, $\varepsilon n^2\sigma T^4$

Numerical model

Due to the complexity of the mini-oven geometry and presence of the non-linear effects ($q_r \sim T^4$) a heat transfer analysis was performed using the FEM with COMSOL Multiphysics. The oven's 2-D axial symmetry was used in order to speed up the calculation time. The 2-D model geometry was imported from Creo Parametric via d*xf* format. The FEM-mesh features 51709 6-node Lagrangian triangle plane elements forming fixed mesh. The mesh quality is based on the ratio of the area to the sum of the square of edge lengths for 2-D elements. A value of 1 indicates a perfect square, while 0 indicates that the element has zero area. In the present model, the average element quality is over 0.975.

The axial mini-oven cross-section is shown in fig. 5(a) cross-section of mini-oven and fig. 5(b) enlarged view of contacts important for heat transfer calculations. The parts made out of different materials are presented in different colors. The total length of the simulation model was 282 mm. We assumed mini-oven being in a vacuum inside the tube made of stainless steel with a diameter of 100 mm. The temperature on the outer wall was set to 20 °C. As one can observe from the fig. 5(b), there are four boundary contact surfaces between elements of a mini-oven that should be taken into consideration. Other surface contacts are loose and were neglected in the simulation. Three out of four contact surfaces have a higher value of axial contact pressure, due to tightening of oven's body parts. Out of these three contacts, two, Contacts 3 and 4 in fig. 5(b), are between alumina and molybdenum with h_c coefficient estimated at 75 kW/m^{2}K, while the third one, Contact 2 in fig. 5(b), between alumina and tantalum has its h_c coefficient estimated at 56 kW/mK. The final contact, Contact 1 in fig. 5(b), between stainless steel and tantalum, is threaded connection and has only radial pressure with h_c coefficient estimated at 10 kW/mK.

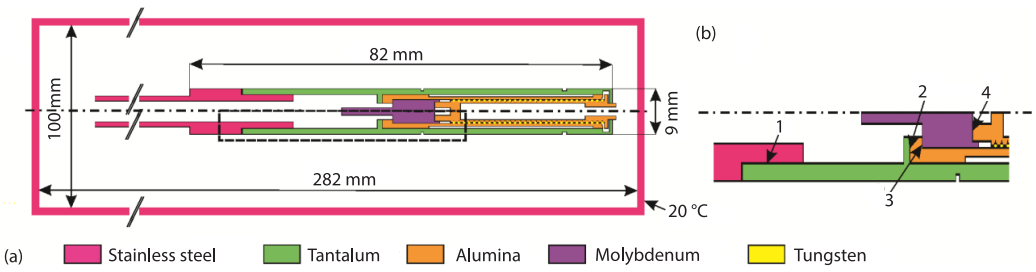

Figure 5. The axial cross-section of FAMA mini oven; (a) the entire mini-oven and (b) enlarged contact surfaces important for heat transfer (*for color image see journal web site*)

Algorithm for solving radiative heat flux

Surface-to-surface Radiation Interface in COMSOL calculates incident radiation flux that comes on the specific diffuse surface as a sum of all other irradiation fluxes coming from other diffuse surfaces, G^i_m, plus the one coming from the ambient, $G_{amb} = \varepsilon\sigma T^4_{amb}$.

The radiosity solver computes view factors between diffuse surfaces that irradiate each other. Loosely speaking, a view factor is a measure of how much influence the radiosity emitted from a given part of the boundary has on the radiation received at some other part. Consider a Point P on a surface as in fig. 6. The mutual irradiation at Point P originating from the surfaces S_1 is given by the following surface integral:

$$G^1_m(J_1) = \int_{S_1}^{2} \frac{\left(-\vec{n}_1 \cdot \vec{r}\right)\left(\vec{n} \cdot \vec{r}\right)}{\pi |r|^4} J_1 \mathrm{d}s \tag{10}$$

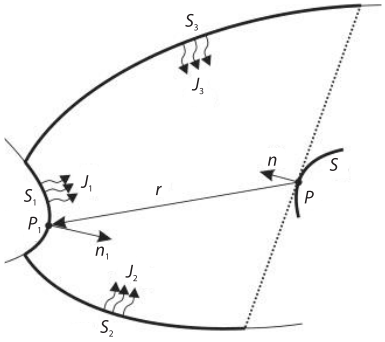

Figure 6. Geometry for the determination of the view factor in surface-to-surface radiation

The heat flux that arrives from Point P_1 depends on the local radiosity J_1 projected on Point P. The projection is computed using the normal vectors $\vec{n}$ and $\vec{n}_1$ along with the vector $\vec{r}$, which Points from P to P_1, fig. 6. On the other hand, F_{amb} is the view factor of the ambient portion of the field of view, which is considered to be a single boundary with constant radiosity. Its value is equal to the fraction of the field of view that is not covered by other boundaries. Using eq. (9) we get for radiosity, as a function of $G_m(J)$, implicit radiation equation:

$$J = (1-\varepsilon)\left[G_m(J) + F_{\text{amb}} T_{\text{amb}}^4\right] + \varepsilon\sigma T^4 \tag{11}$$

Equation (11) is the base for iterative procedure repeated until convergence of radiosity value for specific diffuse surface is achieved.

Materials

In order to determine temperature distribution in steady-state, a knowledge of thermal conductivity, k, and material emissivity, ε, eq. (1), is needed. These properties are temperature-dependent. Since temperature dependence of thermal conductivity, k, for all materials of interest is not significant in the temperature range in question, 900-2000 K ~ (600-1700 °C), fig. 7(a), for each material, we have taken it to be equal to the value at expected temperature level for that material [14-16].

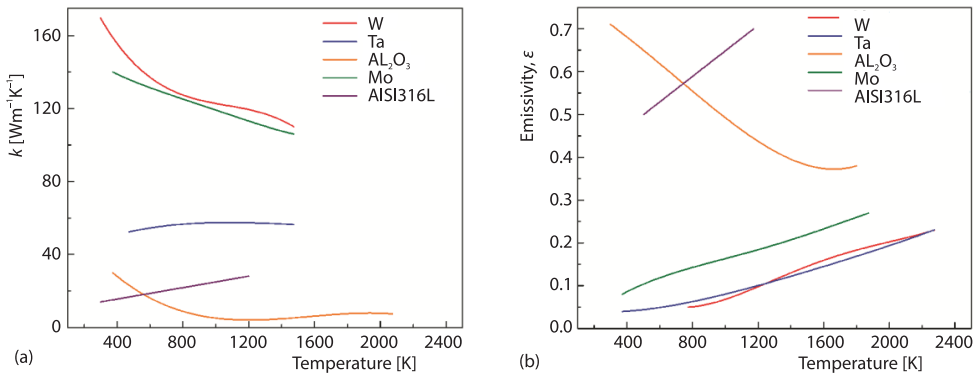

Figure 7. Thermal conductivity (a) and emissivity (b) *vs.* temperature curves for mini-oven building materials (*for color image see journal web site*)

The thermal conductivity values used in FEM calculations are shown in tab. 1. Material emissivity, ε, strongly depends on surface conditions. Available data for both, materials with heavily oxidized surfaces and polished materials with non-oxidized surface, could be found in [17-19]. By fitting these data with polynomials of third-degree, a $\varepsilon(T)$ dependence in analytical form was obtained tab. 1 shown in fig. 7(b).

Table 1.Thermal conductivity, k, and emissivity $\varepsilon(T) = a + bT + cT^2 + dT^3$ of materials used in numerical temperature calculations of FAMA mini-oven

Material	k [Wm^{-1}K^{-1}]	a	b	c	d
Tungsten (W)	173	0.052	$-1.166 \cdot 10^{-7}$	$1.818 \cdot 10^{-7}$	$4.228 \cdot 10^{-11}$
Tantalum (Ta)	57	0.034	$8.294 \cdot 10^{-6}$	$6.444 \cdot 10^{-8}$	$1.007 \cdot 10^{-11}$
St. steel (AISI 316L)	21	0.351	$2.972 \cdot 10^{-4}$	0	0
Molybdenum (Mo)	138	0.031	$1.353 \cdot 10^{-4}$	$-1.359 \cdot 10^{-8}$	$4.941 \cdot 10^{-12}$
Alumina (Al_2O_3)	6	0.776	$6.875 \cdot 10^{-5}$	$3.598 \cdot 10^{-7}$	$1.529 \cdot 10^{-10}$

Heat sources

The mini-oven heat is generated through the electrical dissipation. The generated Joule power P_{Joul} is given:

$$P_{\text{Joul}} = \rho \frac{l}{S} I^2 \tag{12}$$

where l is conductor length, S – the conductor cross-section area, ρ – the specific electrical resistivity of a material, and I – the current through electrical circuit. The diagram of heating power generating electrical assembly is shown in fig. 8.

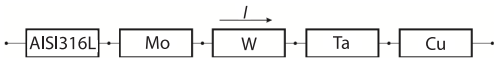

Figure 8. Mini-oven's heating power generating electrical assembly

It consists out of a copper conductor, molybdenum connectors, a tungsten filament, a tantalum made oven body and stainless-steel cane attached to the oven back side. Since the same current flows through all parts, the dissipated heating power ratios can be easily calculated. The heating power contributions of each part of electrical assembly at room and expected temperature in the steady-state are presented in tab. 2 together with temperature corrected heating power contributions.

Table 2. Power distribution ratios (PDR) at room and near steady-state temperatures

Conductor	CS area, S [mm^2]	Length, l [mm]	Resistivity, R_0 [Ω]	*PDR* $R_0/R\Sigma$ [%]	Temperature, T_{ss} [°C]	Resistivity, R [Ω]	*PDR* $R/R\Sigma$ [%]
Copper	0.79	1100	0.0234	6.3	400	0.0609	2.1
Molybdenum	7.07	20	0.0001	0.0	900	0.0008	0.0
Tungsten	0.07	380	0.3037	81.3	1700	2.7429	95.6
Tantalum	29.40	85	0.0004	0.1	800	0.0014	0.0
AISI 316L	17.62	1100	0.0462	12.4	400	0.0624	2.2

The highest contribution the heating power dissipation comes from the tungsten filament, 0.3 mm in diameter, varying from 81-96% in the room temperature, to 1700 °C, temperature range, respectively. Therefore, we assumed that the all of the heat is being generated in tungsten filament, while all other parts of mini-oven are being heated only by mutual heat exchange mechanisms described in section *Heat transfer mechanismus*.

Results and discussion

The temperature calculations were performed with the heat transfer module of COMSOL Multiphysics software package. In the calculations the heating source of the FAMA mini-oven, a tungsten filament made out of 30 winds, is represented as 30 independent ring-like heat sources. Location of the highest temperature in the mini-oven is found to be at the 5th filament winds from the gas outlet side. Two additional temperature points of interest have been chosen: one on the inner surface in the middle of the alumina made crucible and second one at the corresponding location on the outer surface of the tantalum made oven body. In these three points the temperature *vs*. heating power dependence has been observed, fig. 9. Maximum value of 25 W of heating power is determined upon the numerically calculated maximum temperature value of 1660 °C on the 5th filament winds. This value of temperature is bellow aforementioned temperature limit for chemical stability between tungsten filament and alumina crucible. Furthermore, the temperature exhibits $\sim P^{1/4}$ dependence with heating power, in clear reference to the Stefan-Boltzmann radiation law. Henceforth, for mini-oven's working temperature range, the radiation is a highly dominant mechanism of heat transfer.

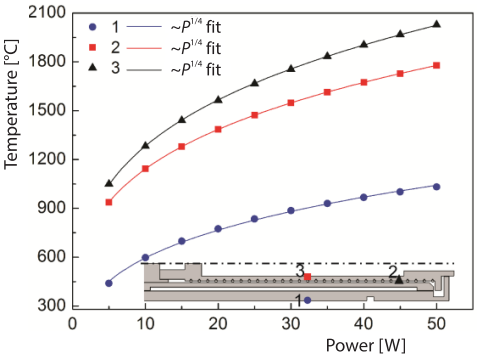

Figure 9. Temperature *vs*. heating power dependence calculated for three points shown

The temperature distribution of FAMA mini-oven for 25 W of heating power is shown in fig. 10. We can observe that the highest temperature (1660 °C) is generated on the tungsten filament. Going radially inside, towards the crucible, the temperature decreases to about 1400 °C at the inner crucible wall. This temperature is maintained along the crucible relatively uniformly, except at its tail ends where the temperature drop is considerable more so at the gas outlet side with 400 °C fall. The outer surface of the mini-oven's body in the length of crucible is significantly cooler with temperatures in the 750-830 °C range, denoting that the most of heat flux is confined within the crucible. Further away from the crucible, along oven's axis, one can observe the rapid temperature drop, which further declines in the oven's cane area, enabling mini-oven handling.

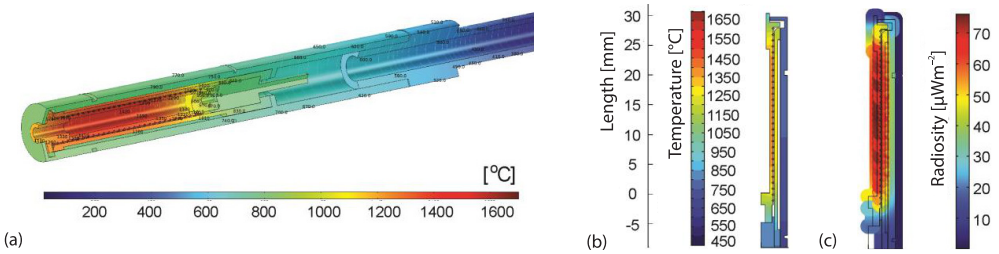

Figure 10. (a) Temperature distribution inside the FAMA mini-oven for 25 W of heating power, (b) temperature, and (c) radiosity distribution along axial cross-section of FAMA mini-oven powered by 25 W

Figure 10(b) shows also temperature and fig. 10(c) radiosity distribution along axial cross-section of mini-oven powered by 25 W. As it was mentioned previously, temperature quasi-uniformity within the crucible along the most of its length is clearly seen. Also, a very good

confinement of radiosity within the crucible is observed, resulting in high temperatures in the crucible in comparison with the rest of the mini-oven. There is a dominant radiosity flow along axial direction, denoted with a smooth color transition. The increase of radiosity at the mini-oven's gas outlet compared to the opposite side of the crucible is a result of the edge effect [20].

The calculated temperature along inner crucible surface is presented at fig. 11, the red line – 1. The bolded lines – 3 on mini-oven simulation axisymmetric 2-D model cross-section represent the crucible's edge for which temperature dependence on crucible length is presented. As it can be observed, within the majority of crucible, in the range between 5 and 25 mm, or nearly 71% of its entire length, the temperature is relatively stable, with a relative change no worse than 4%. Outside of this region we have temperature drops, with the one at the gas outlet side being more pronounced, ~400 °C or 23% drop. These temperature drops could cause a serious reduction of the oven performance, since they could lead to deposition of evaporated material on the gas outlet. This problem could be somewhat mitigated with the heating power density redistribution along the filament. A better temperature distribution along the crucible, fig. 11, the black line – 2, could be obtained if the filament heating power density in the area marked by dashed rectangle is increased by 60%, compared to the uniform one, while maintaining the 25 W on the filament. This leads to 9% lower heating power density on the rest of the filament. Further increase of heating power density would result in higher maximum temperature than chemically allowed (1700 °C). The newly obtained temperature distribution has a wider temperature plateau, extending further into gas outlet side of the crucible. Also, it has a lesser temperature drop (~300 °C). The heating power redistribution shifts filament's radiosity towards the gas outlet side of the crucible, resulting in more asymmetric temperature distribution. However, the range in which temperature varies is within 4% of its maximum value is increased by 2 mm, ranging now from 5.5-27.5 mm, increasing the region of temperature quasi-uniformity by 7%. The aforementioned power redistribution could be achieved twofold: either by increasing the filament winding density in the marked region, or by having two filaments powered by different currents. We have used the latter option in our numerical simulation.

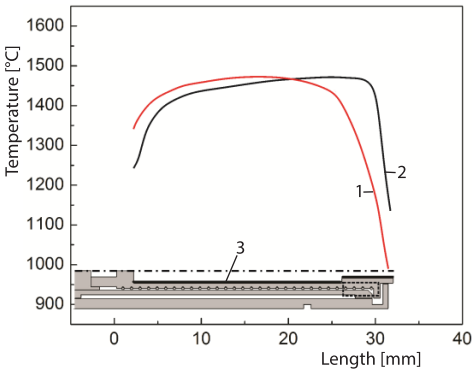

Figure 11. The calculated temperature along alumina crucible surface for 25 W of heating power: 1 – with the uniform heating power density distribution and 2 – with 60% heating power increase within region marked with dashed rectangle

Conclusion

We used numerical FEM to calculate temperature distribution of mini-oven designed for FAMA installation ECR ion source, in the steady-state working regime. It was found that filament power of 25 W gave the maximum temperature of 1660 °C, below a limiting temperature for the system. The thermal radiation has been shown to be the dominant heat exchange mechanism within the mini-oven. The FEM analysis points out to a very good axial temperature quasi-uniformity along 71% of the length of mini-oven's crucible, inside which the temperature changes in 4% range of its maximum value. The region of temperature quasi-uniformity could be further extended by additional 7% with a heating power redistribution, putting a greater emphasis on powering the filament in the gas outlet region. The power redistribution also results in less pronounced temperature drop (25%) in the same region.

The calculations for heat exchange were based on emissivity data for polished and cleaned surfaces for some materials used in the design. However, the emissivity strongly depends on the state of the surface of the radiating material, including oxidation effect, which is main unknown quantity in advance. Henceforth, in our future study, we will compare the simulation results with the experimentally measured temperatures in order to improve our numerical model.

Acknowledgment

Igor N. Telečki, Ljubiša T. Vukosavljević, Ivan M. Trajić, Marko V. Erich, and Viktor N. Jocić the research was funded by the Ministry of Education, Science and Technological Development of the Republic of Serbia (research topic *Physics and chemistry with ion beams*).

References

[1] Dobrosavljević, A., *et al*., A Channel for Modification of Materials with Post-Accelerated or Decelerated Multiply Charged Ion Beams, *Nucl. Instrum. Meth. A*, *597* (2008), 2-3, pp. 136-141
[2] Efremov, A. A., *et al*., Design Aspects and Status of Construction of the mVINIS Ion Source, *Rev. Sci. Instrum*., *69* (1998), 2, pp. 679-681
[3] Dobrosavljević, A., *et al*., Progress Report on the mVINIS Ion Source, *Rev. Sci. Instrum*., *72* (2000), 2, pp. 915- 917
[4] Dobrosavljević, A., *et al.*, Recent Results with the mVINIS Ion Source, *Rev. Sci. Instrum*., *75* (2004), 5, pp. 1460-1462
[5] Efremov, A. A., *et al*., Upgrading the ECR Ion Source Within Fama, *Nucl. Technol. Radiat. Prot*., *33* (2018), 1, pp. 47-52
[6] Loginov, V. N., *et al*., Production of Intense Metal Ion Beams at the DC-60 Cyclotron, *Journal Instrum*., *2* (2019), 14, pp. 55-62
[7] Koivisto, H., *et al*., The First Results with the New JYFL 14 GHz ECR Ion source, *Nucl. Instrum. Meth. B*, *174* (2001), 3, pp. 379-384
[8] Jovović, J., *et al*., Mivoc Method at the mVINIS Ion Source, *Nucl. Technol. Radiat. Prot*., *22* (2007) 2, pp. 10-14
[9] Loginov, V. N., *et al*., Production of Intense Beams of Lithium, Magnesium, Phosphorus and Calcium Ions by ECR Ion Source at DC-60 Cyclotron, *Physics of Particles and Nuclei Letters*, *16* (2019), 1, pp. 30-33
[10] ***, PANTECHNIK, PK10-0501-DT04/Oven Head Technical Datasheet, /https://www.pantechnik.com
[11] Koivisto, H., *et al*., Development of Metal Ion Beams and Beam Transmission at JYFL, *Proceedings*, HIAT09, Venice, Italy, 2009
[12] ***, Comsol-Multiphysics, https://www.comsol.com
[13] Cooper, M. G., *et al*., Thermal Contact Conductance, *International Journal of Heat and Mass Transfer*,*12* (1969), 3, pp. 279-300
[14] David, R., The *CRC Handbook of Chemistry and Physics*, (Ed. Lide), CRC Press, Taylor and Francis, Boca Raton, Fla., USA, ,2009
[15] Choong, S. K., *Thermophysical Properties of Stainless Steels*, Argonne National Laboratory, Argone, Ill., USA, 1975
[16] ***, Plansee, https://www.plansee.com
[17] Michael, F., *Radiative Heat Transfer*, Academic Press, New York, USA, 2013
[18] Whitson, M. E., *Handbook of the Infrared Optical Properties of Al_2O_3, Carbon, MGO and ZrO_2*, AEROSPACE CORP., DTIC, Fort Belvoir, Va., USA, 1975
[19] John, H. L. IV, John H. L. V, *A Heat Transfer Textbook*, Phlogiston Press, Cambridge. Mass., USA, 2008
[20] Bejan, A., Kraus, A. D., *Heat Transfer Handbook*, John Wiley & Sons, New York, USA, 2003

Paper submitted: May 19, 2021
Paper revised: June 5, 2021
Paper accepted: June 28, 2021